Reducing computational effort in topology optimization considering the deformation in additive manufacturing.

Takao Miki[a,*]

[a]*Osaka Research Institute of Industrial Science and Technology, 7-1, Ayumino-2, Izumi-city, Osaka, 594-1157, Japan*

Abstract

Integrating topology optimization and additive manufacturing (AM) technology can facilitate innovative product development. However, laser powder bed fusion, which is the predominant method in metal AM, can lead to issues such as residual stress and deformation. Recently, topology optimization methods considering these stresses and deformations have been proposed; however, they suffer from challenges caused by an increased computational cost. In this study, we propose a method for reducing computational cost in topology optimization considering the deformation in AM. An inherent strain method-based analytical model is presented for simulating the residual stress and deformation in the AM process. Subsequently, a constraint condition to suppress the deformation is formulated, and a method to reduce the computational cost of the adjoint analysis in deriving sensitivity is proposed. The minimum mean compliance problem considering AM deformation and self-support constraints can then be incorporated into the level set-based topology optimization framework. Finally, numerical examples are presented for validating the effectiveness of the proposed topology optimization method.

Keywords: Topology optimization, Level set method, Laser powder bed fusion (metal additive manufacturing), Design for additive manufacturing, Computational cost, Inherent strain method

*Corresponding author
Email address: mikit@orist.jp (Takao Miki)

1. Introduction

Additive manufacturing (AM) processes can fabricate complex geometric parts by repeating the process of building up materials and be expected to further improve product performance. In recent years, several research studies have focused on innovative manufacturing combined with topology optimization, which is a powerful design tool that can exploit the advantages of the features of this manufacturing technique.

A prevalent method in metal AM is laser powder bed fusion (LPBF), which can construct three-dimensional objects by sequentially melting and solidifying metal powder using a laser in a layer-by-layer manner. Despite its widespread use, LPBF suffers from several manufacturing challenges, including overhang limitation, residual stress, distortion, and overheating. Support structures are often required for mitigating issues compromising dimensional accuracy and inducing manufacturing defects. However, these structures are not ideal because they elevate manufacturing and post-processing costs because of their removal.

Topology optimization methods that can address these manufacturing challenges of AM have been developed actively. Topology optimization methods that can incorporate overhang constraints have received considerable attention within these challenges [1, 2, 3, 4, 5, 6, 7, 8, 9]. A common strategy involves integrating geometrical constraints for creating self-supporting structures, minimizing their need for support structures and associated costs. However, this strategy cannot adequately address physical issues such as residual stress and deformation.

Several topology optimization approaches have been explored to consider residual stress, deformation, and overheating [10, 11, 12, 13, 14, 15, 16, 17]. These methods can circumvent physical challenges by integrating AM process models, and they can be categorized into the thermo-mechanical analysis [18, 19, 20, 21, 22, 23, 24] and inherent strain methods [25, 26, 27, 28, 29]. The former employs a coupled transient thermal and mechanical analysis for forecasting component overheating, residual stress, and deformation. The latter predicts residual stress and deformation using an inherent strain derived from the thermo-mechanical analysis or experimental data; however, it does not consider overheating caused by the absence of thermal information. The main advantage lies in its lower computational demand.

Some topology optimization methods consider multiple manufacturability factors, thereby merging geometrical constraints with AM process models.

Miki [30] proposed a level-set-based topology optimization method that incorporates overhang and deformation constraints. Xu et al. [31] proposed a density-based topology optimization method with overhang and residual stress constraints. Both approaches utilize a simplified inherent strain method that excludes plastic deformation considerations; however, they are computationally intensive because of iterative calculations required to optimize residual stress or deformation in the AM process, thereby necessitating layer-by-layer mechanical and adjoint analyses.

A potential solution for reducing computational burden involves increasing the macro layer size in the AM process model, decreasing the number of layers. Although this approach decreases the computational load of the mechanical and adjoint analyses, it also affects the accuracy of residual stress and deformation predictions. To overcome this limitation, we propose a method for reducing computational costs while preserving prediction accuracy. This is achieved by streamlining the adjoint analysis to a single calculation, focusing on the adjoint problem associated with the final state of the construction process of AM, instead of each intermediate state.

The remainder of this paper is organized as follows. Section 2 describes the level-set-based topology optimization method. In Section 3, we present the AM process model based on the inherent strain method and a physical model representing the final state of the AM building process. Subsequently, the formulation of the constraint function for physical challenges in AM is introduced. In Section 4, the self-support constraint based on the combination of geometrical and thermal constraints are formulated. Then, we formulate an optimization problem that considers multiple challenges of the AM process in Section 5, and construct an optimization algorithm using the finite element method (FEM) in Section 6. Section 7 presents the 2D and 3D numerical examples used for validating the utility of the proposed method. Finally, Section 8 provides the conclusions.

2. Level-set-based topology optimization

The basic concept of topology optimization involves replacing the structural optimization problem with a material distribution problem, wherein the presence or absence of a material is determined within a fixed design domain $D \subset \mathbb{R}^N (with N = 2 \, or \, 3)$. The fixed design domain D is differentiated into the material domain Ω and void domain $D \backslash \Omega$ using a characteristic function. The level set method expresses the structural boundary $\partial\Omega$ between the ma-

terial and void domains using an iso-surface of a scalar function called the level set function. In this study, topology optimization [32] performed using the reaction-diffusion equation is employed to update the level set function, which is defined as follows:

$$\begin{cases} 0 < \phi(\boldsymbol{x}) \leq 1 & \text{for } \boldsymbol{x} \in \Omega \\ \phi(\boldsymbol{x}) = 0 & \text{for } \boldsymbol{x} \in \partial\Omega \\ -1 \leq \phi(\boldsymbol{x}) < 0 & \text{for } \boldsymbol{x} \in D \backslash \Omega. \end{cases} \tag{1}$$

The characteristic function is represented using the level-set function ϕ as follows:

$$\chi_\phi = \begin{cases} 1 & \text{for } \phi(x) \geq 0 \\ 0 & \text{for } \phi(x) < 0, \end{cases} \tag{2}$$

based on Eq. 2, the level-set-based optimization problem is formulated as follows:

$$\begin{aligned} &\inf_{\phi} \quad J\left(u, \chi_\phi\right) \\ &\text{subject to:} \quad \text{governing equations for} \quad u \end{aligned} \tag{3}$$

where J and u represent an objective function and a state variable, respectively. Then, the optimal material distribution χ_ϕ, i.e., the distribution of the level-set function ϕ, is determined by solving a time-evolution equation, where a fictitious time s is introduced as follows:

$$\frac{\partial \phi(s)}{\partial s} = -K(\tilde{C}J' - \tau\nabla^2\phi), \tag{4}$$

$$\tilde{C} := \frac{C \int_D \mathrm{d}\Omega}{\int_D |J'| \, \mathrm{d}\Omega}. \tag{5}$$

where $K \in \mathbb{R}^+$, $C \in \mathbb{R}^+$, J', and $\tau \in \mathbb{R}^+$ represent a proportional coefficient, normalization coefficient, design sensitivity of the target optimization problem, and a regularization parameter, respectively. The design sensitivity is derived based on an adjoint variable method. In this study, we set $K = 1.0$, $C = 0.8$, and $\tau = 5.0 \times 10^{-4}$.

3. AM process model and deformation constraint

The inherent strain method is widely used to predict residual stress and deformation in welding. The AM process can be considered an iterative

welding process, and therefore, the inherent strain method is applicable. The residual stress is attributed to inelastic strains such as thermal, plastic, and phase transformation strains, which are generated during the local melting and solidification processes of the metal powder. The sum of these inelastic strains is called the inherent strain $\boldsymbol{\varepsilon}^{inh}$, and the total strain $\boldsymbol{\varepsilon}(\boldsymbol{u}) := \frac{1}{2}(\nabla \boldsymbol{u} + (\nabla \boldsymbol{u})^{\top})$ is composed of elastic strain $\boldsymbol{\varepsilon}^{el}$ and inherent strain $\boldsymbol{\varepsilon}^{inh}$ as follows:

$$\boldsymbol{\varepsilon}(\boldsymbol{u}) = \boldsymbol{\varepsilon}^{el} + \boldsymbol{\varepsilon}^{inh}. \tag{6}$$

We consider a part Ω divided into m macro-layers with a fixed layer thickness in the building direction to apply the inherent strain method to the AM building process shown in Fig. 1. Ω_p represents the printed domain and

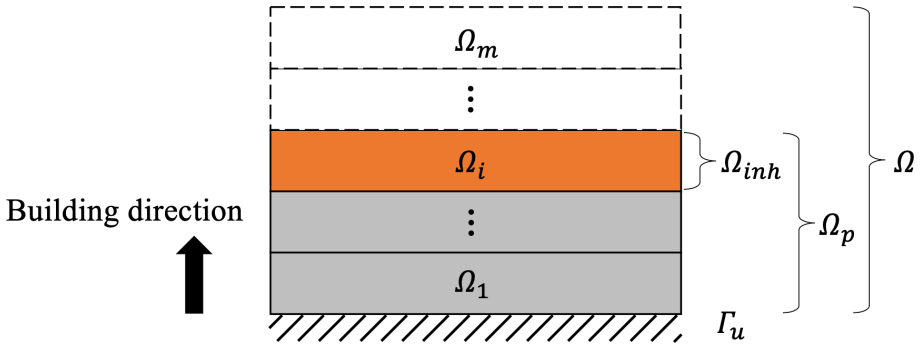

Figure 1: Domains and boundaries of the mechanical model in the building process.

Ω_{inh} represents the layer Ω_i at the top of the printed domain Ω_p, where the inherent strain is imposed. The printed domain Ω_p is defined by domain Ω_i, $1 \leq i \leq m$ as follows:

$$\Omega_p = \Omega_1 \cup \ldots \cup \Omega_i. \tag{7}$$

This study employs a linear inherent strain problem that does not consider plastic deformation [12, 31, 33]. Ω_p is occupied by an isotropic elastic material. The bottom surface Γ_u of the part is clamped and Ω_{inh} is loaded with the inherent strain. The displacement field $\boldsymbol{u}_i \in H^1(\Omega_p)^N$ is represented by

the following governing equation:

$$\begin{cases} -\mathrm{div}(\boldsymbol{\sigma}_i) = 0 & \text{in } \Omega_p \\ \boldsymbol{\sigma}_i = \mathbb{D}(\boldsymbol{\varepsilon}(\boldsymbol{u}_i) - \boldsymbol{\varepsilon}^{inh}), & \\ \boldsymbol{u}_i = \boldsymbol{0} & \text{on } \Gamma_u \\ -\boldsymbol{\sigma}_i \cdot \boldsymbol{n} = \boldsymbol{0} & \text{on } \partial\Omega_p \setminus \Gamma_u, \end{cases} \tag{8}$$

for all indices $i = 1, 2, \ldots, m$, where $\boldsymbol{\sigma}$ and $\mathbb{D}$ represent the stress tensor and isotropic elasticity tensor, respectively. The inherent strain $\boldsymbol{\varepsilon}^{inh}$ in Ω_{inh} is defined as follows:

$$\boldsymbol{\varepsilon}^{inh}(\boldsymbol{x}) = \begin{cases} \boldsymbol{\varepsilon}^{inh} & \text{for } \boldsymbol{x} \in \Omega_{inh}, \\ \boldsymbol{0} & \text{otherwise }, \end{cases} \tag{9}$$

The inherent strain vector $\boldsymbol{\varepsilon}^{inh}$ has six components $[\varepsilon_x^{inh} \quad \varepsilon_y^{inh} \quad \varepsilon_z^{inh} \quad \varepsilon_{xy}^{inh} \quad \varepsilon_{yz}^{inh} \quad \varepsilon_{zx}^{inh}]^{\mathsf{T}}$. In this study, the in-plane strain component $\varepsilon_x^{inh}, \varepsilon_y^{inh}$ is assumed to be constant, and the building direction ε_z^{inh} and shear strain components $\varepsilon_{xy}^{inh}, \varepsilon_{yz}^{inh}, \varepsilon_{zx}^{inh}$ are omitted [34, 26]. Part-scale residual stress and distortion can be calculated by applying inherent strain $\boldsymbol{\varepsilon}^{inh}$ to each domain Ω_{inh} from $i = 1$ to m. The inherent strain component is determined by a high-fidelity analysis such as a thermo-mechanical analysis or by partial cutting a cantilever-shaped specimen and measuring the resulting deformation. For details on the algorithm of the building process and identification of inherent strain $\boldsymbol{\varepsilon}^{inh}$ using FEM, please refer to Miki et al. [12]. The residual stress $\boldsymbol{\sigma}$ and deformation $\boldsymbol{u}$ after completing the building process are obtained by summing the layer-wise residual stress $\boldsymbol{\sigma}_i$ and deformation $\boldsymbol{u}_i$ as follows:

$$\boldsymbol{u} = \sum_{i=1}^{m} \boldsymbol{u}_i \qquad \text{for } \boldsymbol{x} \in \Omega_p, \tag{10}$$

$$\hat{\boldsymbol{\varepsilon}}^{el} = \sum_{i=1}^{m} (\boldsymbol{\varepsilon}(\boldsymbol{u_i}) - \boldsymbol{\varepsilon}^{inh}) \qquad \text{for } \boldsymbol{x} \in \Omega_p, \tag{11}$$

$$\boldsymbol{\sigma} = \sum_{i=1}^{m} \boldsymbol{\sigma}_i = \mathbb{D}\hat{\boldsymbol{\varepsilon}}^{el} \qquad \text{for } \boldsymbol{x} \in \Omega_p. \tag{12}$$

Based on these equations, the inherent strain $\hat{\boldsymbol{\varepsilon}}^{inh}$ on the entire part Ω can be derived as follows:

$$\hat{\boldsymbol{\varepsilon}}^{inh} = \boldsymbol{\varepsilon}(\boldsymbol{u}) - \hat{\boldsymbol{\varepsilon}}^{el}. \tag{13}$$

Using the inherent strain $\hat{\boldsymbol{\varepsilon}^{inh}}$, the displacement field $\hat{\boldsymbol{u}}$ of the final state is expressed by the following governing equation:

$$\begin{cases} -\mathrm{div}(\boldsymbol{\sigma}) = 0 & \text{in } \Omega \\ \boldsymbol{\sigma} = \mathbb{D}(\boldsymbol{\varepsilon}(\hat{\boldsymbol{u}}) - \hat{\boldsymbol{\varepsilon}}^{inh}) & \\ \hat{\boldsymbol{u}} = \boldsymbol{0} & \text{on } \Gamma_u \\ -\boldsymbol{\sigma} \cdot \boldsymbol{n} = \boldsymbol{0} & \text{on } \partial\Omega \setminus \Gamma_u, \end{cases} \tag{14}$$

For deriving the design sensitivity, previous studies solved the adjoint equations corresponding to the governing equations of each intermediate state, i.e., Eq. 8, whereas this study solves only the adjoint problem corresponding to the governing equation of the final state, i.e., Eq. 14. In other words, the calculation for the number of layers is replaced by a single calculation. The deformation during the building process must be reduced to manufacture parts with high precision in AM. In this study, we use the P-norm function to define the deformation constraint as follows:

$$G_u = \left(\int_\Omega |\hat{\boldsymbol{u}}|^b \ \mathrm{d}\Omega \right)^{1/b}, \tag{15}$$

where $b \geq 2$ represents the penalization parameter set to 5.

The design sensitivity of the AM deformation constraint G_u is performed based on the adjoint variable method. Denoting the adjoint variable corresponding to the state variable $\hat{\boldsymbol{u}}$ by $\boldsymbol{\lambda} \in H^1(\Omega)^N$, the adjoint equation for G_u defined as follows:

$$\begin{cases} -\mathrm{div}(\mathbb{D}\boldsymbol{\varepsilon}(\boldsymbol{\lambda})) = -\left(\int_\Omega |\hat{\boldsymbol{u}}|^b \ \mathrm{d}\Omega \right)^{1/b-1} |\hat{\boldsymbol{u}}|^{b-2} \hat{\boldsymbol{u}} & \text{in } \Omega, \\ \boldsymbol{\lambda} = \boldsymbol{0} & \text{on } \Gamma_u, \\ -(\mathbb{D}\boldsymbol{\varepsilon}(\boldsymbol{\lambda})) \cdot \boldsymbol{n} = \boldsymbol{0} & \text{on } \partial\Omega \setminus \Gamma_u, \end{cases} \tag{16}$$

Then, the design sensitivity is derived as follows:

$$G'_u = -\boldsymbol{\varepsilon}(\hat{\boldsymbol{u}}) : \mathbb{D} : \boldsymbol{\varepsilon}(\boldsymbol{\lambda}) + \boldsymbol{\varepsilon}^{inh} : \mathbb{D} : \boldsymbol{\varepsilon}(\boldsymbol{\lambda}). \tag{17}$$

In addition, for stabilizing the optimization calculation, the sensitivity is averaged for each iteration process as follows:

$$\tilde{G}'_u = (1-\mu)\tilde{G}'^{old}_u + \mu G'_u, \tag{18}$$

where μ represents a parameter that contributes to convergence and $\tilde{G}_u'^{old}$ represents the average sensitivity of the previous iteration. The parameter μ is set to 0.9.

4. Self-support constraint

This chapter describes self-support constraint in a level-set based framework. This self-support constraint consists of an overhang angle constraint and a downward convex shape constraint.

4.1. Overhang angle constraint

In this study, a Helmholtz-type PDE filter is introduced for smoothing the characteristic function χ_ϕ at the structural boundary. The state variable $\psi \in H^1(D)$ and its governing equation are defined as follows:

$$\begin{cases} -aL^2\nabla^2\psi + \psi = \chi_\phi & \text{in} \quad D \\ \boldsymbol{n} \cdot \nabla\psi = 0 & \text{on} \quad \partial\Omega, \end{cases} \tag{19}$$

where $a \in \mathbb{R}^+$, L and $\boldsymbol{n}$ represent the diffusion coefficient that affects the transition width of ψ at the structural boundary, representative length, and outward normal vector, respectively. The coefficient a is set to 1×10^{-4}. Then, the overhang angle θ is evaluated by the inner product of the normal vector of the structural boundary $\partial\Omega$ and building direction vector $\boldsymbol{d}$, as shown in Fig. 2. The overhanging area below the minimum overhang angle θ_0 is represented as follows:

$$\nabla\psi \cdot \boldsymbol{d} \geq |\nabla\psi| \cos\theta_0. \tag{20}$$

From Eq. 20, the condition for constraining the overhang angle is given by

$$G_o = \int_D \sqrt{a}L\mathscr{R}(\nabla\psi \cdot \boldsymbol{d} - |\nabla\psi| \cos\theta_0)\mathrm{d}\Omega, \tag{21}$$

where $\mathscr{R}(s)$ represents the ramp function defined as follows:

$$\mathscr{R}(s) = \begin{cases} 0 & \text{for } s \leq \epsilon_r \\ s & \text{for } s > \epsilon_r \end{cases} \tag{22}$$

where ϵ_r represents a small parameter that limits the area below the minimum overhang angle to only the neighborhood of the structural boundary. The

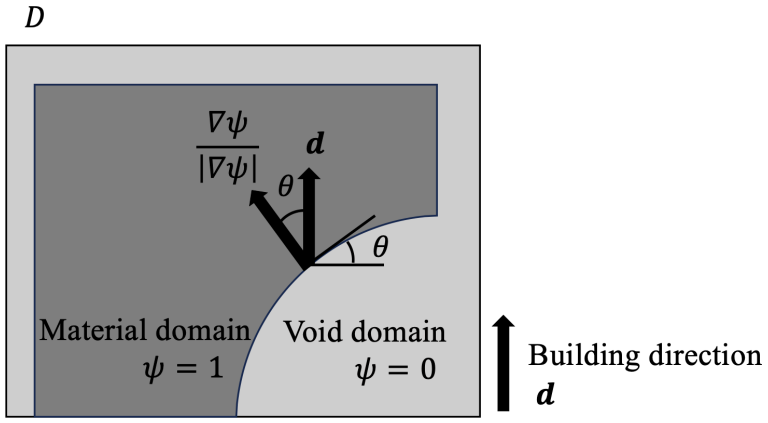

Figure 2: Conceptual diagram of the overhang angle evaluation.

parameter ϵ_r is set to 1×10^{-2}. Then, denoting $p \in H^1(D)$ as the adjoint variable corresponding to the state variable ψ, the adjoint equation for the overhang angle constraint G_o is defined as follows:

$$\begin{cases} -aL^2\nabla^2 p + p = \nabla \cdot \left[\sqrt{a}L\mathscr{H}(\psi)(\boldsymbol{d} - \frac{\nabla\psi}{|\nabla\psi|}\cos\theta_0)\right] & \text{in} \quad D \\ \boldsymbol{n} \cdot \nabla p = 0 & \text{on} \quad \partial\Omega, \end{cases} \tag{23}$$

where $\mathscr{H}(s) := \mathrm{d}\mathscr{R}(s)/\mathrm{d}s$ represents the Heviside function defined as follows:

$$\mathscr{H}(s) = \begin{cases} 0 & \text{for } s \leq \epsilon_r \\ 1 & \text{for } s > \epsilon_r \end{cases} \tag{24}$$

The design sensitivity of G_o is derived as follows:

$$G_o' = -p\chi_\phi. \tag{25}$$

4.2. Downward convex shape constraint

The aforementioned overhang angle constraint creates downward convex shapes that cannot be manufactured. This chapter describes how to suppress the creation of such shapes by introducing a simple thermal model that can simulate the building process [30]. Fig. 3 shows a thermal model that provides the heat flux to the downward structural boundary layer-by-layer. Similar to the inherent strain-based AM process model, part Ω is divided

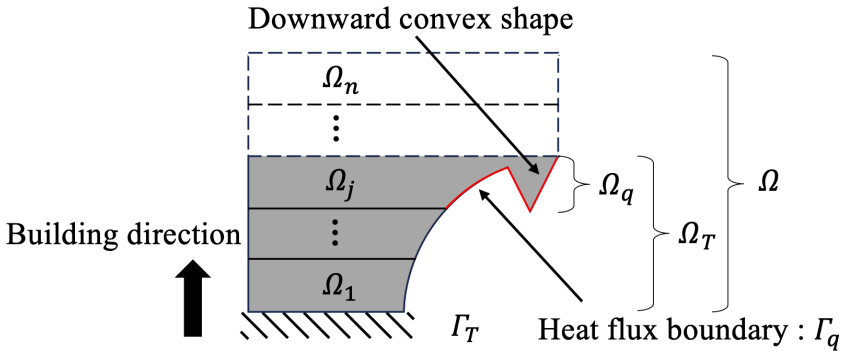

Figure 3: Domains and boundaries of the thermal model in the building process.

into n layers to represent the building process. Domain Ω_T is defined by each domain Ω_j for $1 \leq j \leq n$ and the domain Ω_q is determined by the status of Ω_j. Then, the temperature field $T_j \in H^1(\Omega_T)$ with heat flux Q applied to the overhang boundary Γ_q of the added layer Ω_q is represented by the following governing equation:

$$\begin{cases} \operatorname{div}(k\nabla T_j) = 0 & \text{in } \Omega_T \\ (k\nabla T_j)\cdot \boldsymbol{n} = Q & \text{on } \Gamma_q \\ T_j = T_{amb} & \text{on } \Gamma_T, \end{cases} \tag{26}$$

for all indices $j = 1, 2, \ldots, n$, where T_{amb} represents the base plate temperature. In this thermal model, high temperatures result from shapes obstructing heat flow. To mitigate this, considering the Ω_q heat dissipation of each layer can supress the creation of such shapes. The downward convex shape constraint is defined as follows:

$$G_t = \sum_{j=1}^{n} \int_{\Omega_q} (T_j - T_{amb})^2 \, \mathrm{d}\Omega. \tag{27}$$

Then, denoting the adjoint variable corresponding to the state variable T_j by $q_j \in H^1(\Omega_T)$, the adjoint equation for the downward convex constraint G_t is defined as follows:

$$\begin{cases} \operatorname{div}(k\nabla q_j) = 2\,(T_j - T_{amb}) & \text{in } \Omega_T, \\ (k\nabla q_j)\cdot \boldsymbol{n} = 0 & \text{on } \Omega_T \setminus \Gamma_T, \\ q_j = T_{amb} & \text{on } \Gamma_T, \end{cases} \tag{28}$$

Subsequently, the design sensitivity of G_t is derived as follows:

$$G_t' = \sum_{j=1}^{n} -k\nabla T_j \cdot \nabla q_j. \tag{29}$$

5. Formulation of the optimization problem

In this section, we consider the minimum mean compliance problem with the aforementioned constraints. The material domain Ω comprises of isotropic linear elastic materials. The displacement is fixed at the boundary Γ_v and traction $\boldsymbol{t}$ is imposed on the boundary Γ_t. In the equilibrium state, denoting the displacement field as $\boldsymbol{v} \in H^1(\Omega)^N$, the objective function is given as follows:

$$J_v = \int_{\Gamma_t} \boldsymbol{t} \cdot \boldsymbol{v} \mathrm{d}\Gamma. \tag{30}$$

Under the conditions, the topology optimization problem is formulated as follows:

$$\inf_{\phi} \quad J = J_v + \alpha G_u + \beta G_o + \gamma G_t \tag{31}$$

$$\text{subject to : } E_v = \int_{\Gamma_t} \boldsymbol{t} \cdot \tilde{\boldsymbol{v}} \ \mathrm{d}\Gamma - \int_{\Omega} \varepsilon(\boldsymbol{v}) : \mathbb{D} : \varepsilon(\tilde{\boldsymbol{v}}) \ \mathrm{d}\Omega = 0 \tag{32}$$

$$\text{for } \forall \tilde{\boldsymbol{v}} \in \mathcal{V}, \boldsymbol{v} \in \mathcal{V}$$

$$E_u = \int_{\Omega} \hat{\boldsymbol{\varepsilon}}^{inh} : \mathbb{D} : \varepsilon(\tilde{\boldsymbol{u}}) \ \mathrm{d}\Omega - \int_{\Omega} \varepsilon(\hat{\boldsymbol{u}}) : \mathbb{D} : \varepsilon(\tilde{\boldsymbol{u}}) \ \mathrm{d}\Omega = 0 \tag{33}$$

$$\text{for } \forall \tilde{\boldsymbol{u}} \in \mathcal{U}, \hat{\boldsymbol{u}} \in \mathcal{U}$$

$$E_\psi = -\int_D aL^2 \nabla\psi \cdot \nabla\tilde{\psi} \ \mathrm{d}\Omega - \int_D \psi\tilde{\psi} \ \mathrm{d}\Omega - \int_D \chi_\phi \tilde{\psi} \ \mathrm{d}\Omega = 0 \tag{34}$$

$$\text{for } \forall \tilde{\psi} \in \mathcal{S}, \psi \in \mathcal{S}$$

$$E_t = \int_{\Gamma_q} Q\tilde{T}_j \ \mathrm{d}\Gamma - \int_{\Omega_T} \nabla T_j \cdot \nabla \tilde{T}_j \ \mathrm{d}\Omega = 0 \tag{35}$$

$$\text{for } \forall \tilde{T}_j \in \mathcal{T}, T_j \in \mathcal{T}$$

$$G = \frac{\int_D \chi_\phi \ \mathrm{d}\Omega}{\int_D \ \mathrm{d}\Omega} - V_{\max} \leq 0$$

for all indices $j = 1, 2, \ldots, n$, where α, β, and γ represent the penalization parameters. G and V_{max} represent the volume constraint and upper limit of the volume fraction, respectively. Furthermore, functional spaces $\mathcal{V}$, $\mathcal{U}$, $\mathcal{S}$, and $\mathcal{T}$ are defined as follows:

$$\mathcal{V} := \left\{ \tilde{\boldsymbol{v}} \in H^1(\Omega)^N,\ \tilde{\boldsymbol{v}} = \boldsymbol{0} \ \text{ on } \ \Gamma_v \right\} \tag{36}$$

$$\mathcal{U} := \left\{ \tilde{\boldsymbol{u}} \in H^1(\Omega)^N,\ \tilde{\boldsymbol{u}} = \boldsymbol{0} \ \text{ on } \ \Gamma_u \right\} \tag{37}$$

$$\mathcal{S} := \left\{ \tilde{\psi} \in H^1(D) \right\} \tag{38}$$

$$\mathcal{T} := \left\{ \tilde{T}_j \in H^1(\Omega_T),\ \tilde{T}_j = T_{amb} \ \text{ on } \ \Gamma_T \right\} \tag{39}$$

Since the minimum mean compliance problem is a self-adjoint problem, the design sensitivity is given as follows:

$$J'_v = -\boldsymbol{\varepsilon}(\boldsymbol{v}) : \mathbb{D} : \boldsymbol{\varepsilon}(\boldsymbol{v}). \tag{40}$$

6. Numerical implementation

6.1. Optimization algorithm

The optimization algorithm is given below.

Step 1. The level-set function ϕ is initialized.

Step 2. The governing equations for each state variable are solved by the FEM. In the AM process model, after solving Eq. 8, the inherent strain of the final state is calculated and Eq. 14 is solved.

Step 3. The objective function is computed, and if it converges, the optimization procedure ends.

Step 4. The adjoint equation for each adjoint variable defined is solved using the FEM, and the design sensitivity is computed.

Step 5. The level-set function is updated using the reactiondiffusion equation defined in Eq. 5, and then, the procedure returns to Step 2.

The open-source PDE solver FreeFEM++[35] is used to solve the governing equations.

6.2. Numerical scheme for the governing equation

We describe the ersatz material approach [36] for solving the governing equations. In this study, a small-scaled material property is used to represent the void domain. The boundary between the material and void domains can be smoothly transitioned using a Heaviside function. Subsequently, the extended elastic tensor $\tilde{\mathbb{D}}$ and thermal conductivity $\tilde{k}$ in the fixed design domain D is redefined as follows:

$$\tilde{\mathbb{D}}(\phi; w) = \{(1-c)H_\phi(\phi; w) + c\}\,\mathbb{D} \tag{41}$$

$$\tilde{k}(\phi; w) = \{(1-c)H_\phi(\phi; w) + c\}\,k, \tag{42}$$

where $H_\phi(\phi; w)$ is defined as

$$H_\phi(\phi; w) := \begin{cases} 1 & \text{for } \phi > w, \\ \frac{1}{2} + \frac{\phi}{w}\left(\frac{15}{16} - \frac{\phi^2}{w^2}\left(\frac{5}{8} - \frac{3}{16}\frac{\phi^2}{w^2}\right)\right) & \text{for } -w \le \phi \le w, \\ 0 & \text{for } \phi < -w, \end{cases} \tag{43}$$

where w represents the width of the transition and c represents the scaling parameter of the material properties. Furthermore, Eq. 34 is solved by replacing the characteristic function with this Heaviside function. In our implementation, c is set to 1.0×10^{-3}, w in Eqs. 32, 33, and 35 is set to 0.5, and w in Eqs. 34 is set to 0.9.

Next, an approximate solution method for the heat conduction equation defined in Eq. 35 is introduced. The boundary integral is replaced the domain integral as follows:

$$\int_\Gamma \xi(\boldsymbol{x})\mathrm{d}\Gamma \approx \int_\Omega \xi(\boldsymbol{x})\frac{\mathrm{d}H_\psi(\psi; w)}{\mathrm{d}\psi}|\nabla\psi|\mathrm{d}\Omega. \tag{44}$$

Then, using the inner product of the normal vector $\boldsymbol{n}_\psi := \frac{\nabla\psi}{|\nabla\psi|}$ and building direction $\boldsymbol{d}$, the boundary integral is applied to only the overhang boundary Γ_q as follows.

$$\int_{\Gamma_q} \xi(\boldsymbol{x})\mathrm{d}\Gamma \approx \int_{\Omega_q} \xi(\boldsymbol{x})\frac{\mathrm{d}H_\psi(\psi; w)}{\mathrm{d}\psi}|\nabla\psi|\mathscr{H}(\boldsymbol{n}_\psi \cdot \boldsymbol{d})\mathrm{d}\Omega. \tag{45}$$

7. Numerical examples

7.1. AM deformation constraint

In this section, we verify the effectiveness of the proposed method for reducing the computational cost in the AM deformation constraint. We

compare the previous approach of solving the adjoint equations for each intermediate state of the AM building process with the proposed approach that focuses on only the final state. In all numerical examples, a Young's modulus, Poisson's ratio, and thermal conductivity of 75 GPa, 0.34, 119 W/mK, respectively. In Eq. 8, the in-plane component of the inherent strain $\boldsymbol{\varepsilon}^{inh}$ is set to -0.0025, and the penalization parameter α related to the AM deformation constraint G_u is set to 0.1. Here, we consider a two-dimensional cantilever beam shown in Fig. 4. The upper limit of the volume fraction V_{max} is set to 0.5, and the representative length L is set to 25. In addition, the fixed design domain D is divided in the building direction into 25 layers. The model is discretized by $10,000$ elements with an element size of 1×1 mm. All numerical examples were executed on a workstation equipped with Intel Xeon E5-2687W cores and 512 GB of RAM. Fig. 5 illustrates optimal

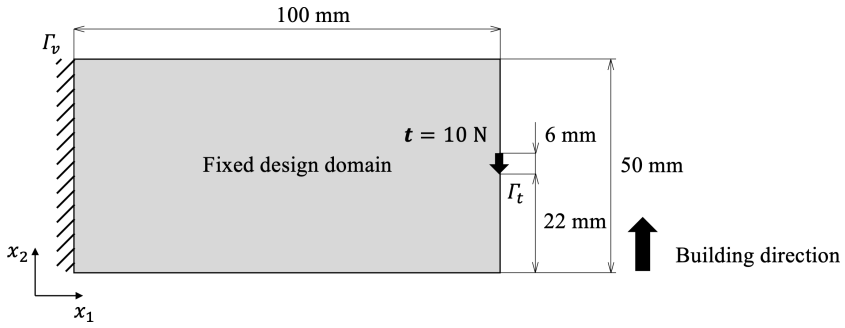

Figure 4: Problem setting for the two-dimensional cantilever beam.

structures obtained through different adjoint analysis methods. The previous method, which involves adjoint analysis for each intermediate state of the building process, is shown in Fig. 5(b). The proposed method, applying adjoint analysis solely to the final state, is depicted in Fig. 5(c). Both optimal structures with the AM deformation constraint have structures that support the overhang area and have the same effect on the compliance. Fig. 6 shows the results of evaluating the deformation induced by the AM building process. Figs. 6(b) and 6(c) demonstrate that the proposed method suppresses deformation as effectively as the previous method. Fig. 7 shows the computational time for each process in the optimization loop. The proposed method increases the computational time for the AM process analysis slightly; however, it significantly reduces the computational time for the ad-

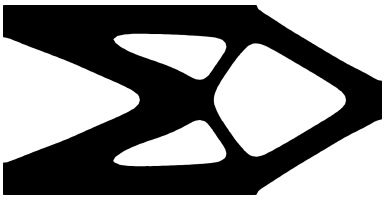

(a) Without constraint; $J_{v\ ref} = 2.52$

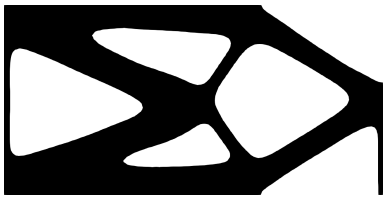

(b) With AM deformation constraint (Previous method); $J_v/J_{v\ ref} = 103\%$

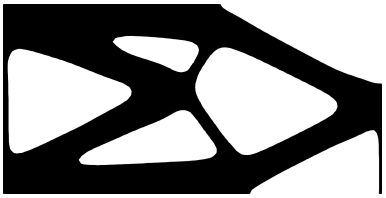

(c) With AM deformation constraint (Proposed method); $J_v/J_{v\ ref} = 103\%$

Figure 5: Optimal structures with and without AM deformation constraint.

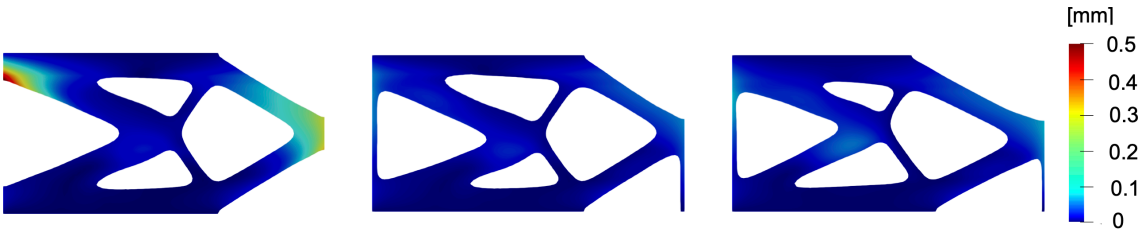

(a) Without constraint

(b) With AM deformation constraint (Previous method)

(c) With AM deformation constraint (Proposed method)

Figure 6: AM deformation for each optimal structure.

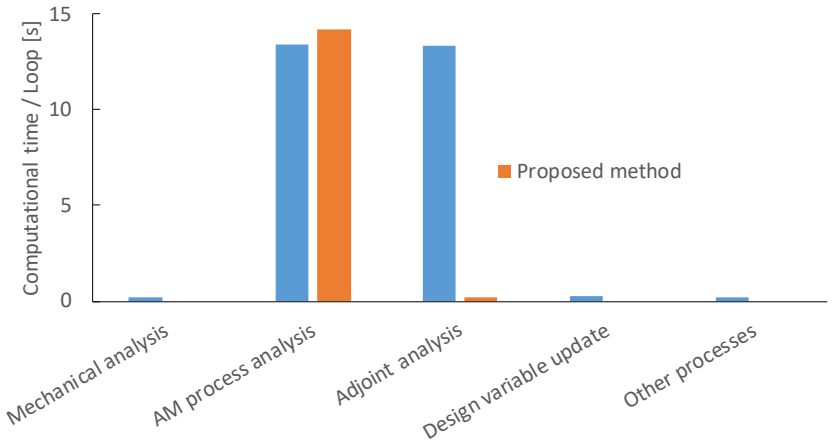

Figure 7: Computational time for each process.

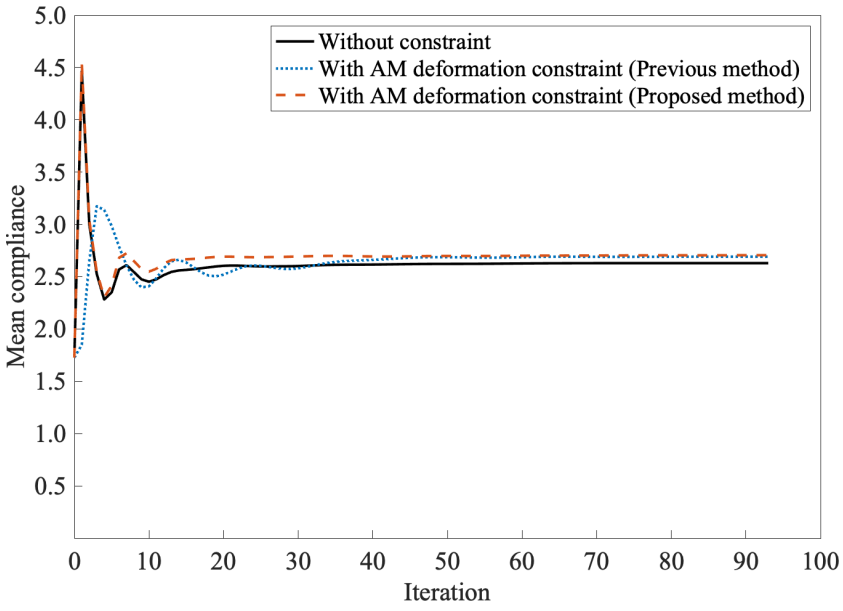

Figure 8: Iteration history of the objective value.

joint analysis. Fig. 8 shows the iterative history of the objective value. The results indicate that the behavior of the objective value changes slightly with a proposed method.

7.2. AM deformation and self-support constraints

This section presents a three-dimensional numerical example that adds the self-support constraint to the AM deformation constraint. Fig. 9 shows the fixed design domain and boundary conditions for a three-dimensional cantilever beam. The upper limit of the volume fraction V_{max} is set to 0.2.

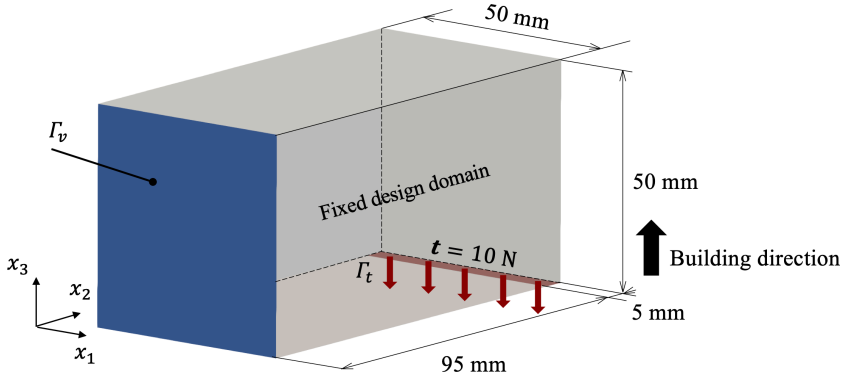

Figure 9: Problem setting for the three-dimensional cantilever beam.

The representative length in Eq. 19 is set to $L = 50$. The minimum overhang angle is set to $\theta_0 = 45°$, and each parameter related to Eq. 26 is set as follows. The heat flux Q is set to 10 W and the base-plate temperature T_{amb} is set to $0/,^\circ C$. The number of layers in the fixed design domain is set to $m = 50$ and $n = 25$ for the AM deformation and downward convex constraints, respectively. The model is discretized by $1,500,000$ elements with an element size of $1 \times 1 \times 1$ mm. In addition, the penalization parameters β and γ the overhand angle and downward convex constraints are set to 0.1 and 0.4, respectively. The other parameters are those set in the previous numerical example.

Figs. 10-12 illustrate the optimal structures under different conditions: without constraints (Fig. 10), with constraints imposed by the previous method (Fig. 11), and with constraints imposed by the proposed method (Fig. 12). The results show that, compared to the unconstrained optimal structure, both constrained optimal structures are self-supporting shapes

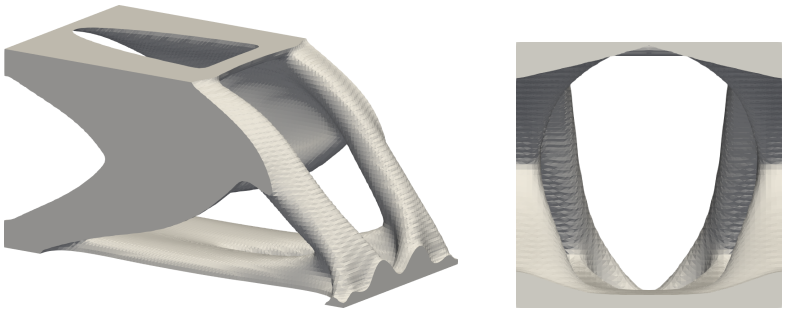

(a) Bird's-eye view (b) Rear view

Figure 10: Optimal structure without constraints; $J_{v\ ref} = 1.09$.

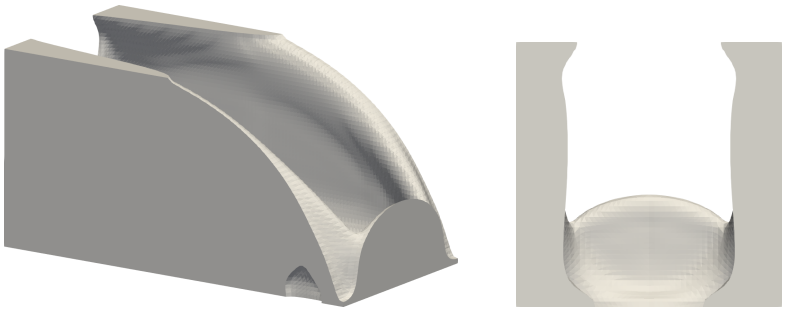

(a) Bird's-eye view (b) Rear view

Figure 11: Optimal structure with the self-support and AM deformation constraints (Previous method); $J_v/J_{v\ ref} = 119\%$.

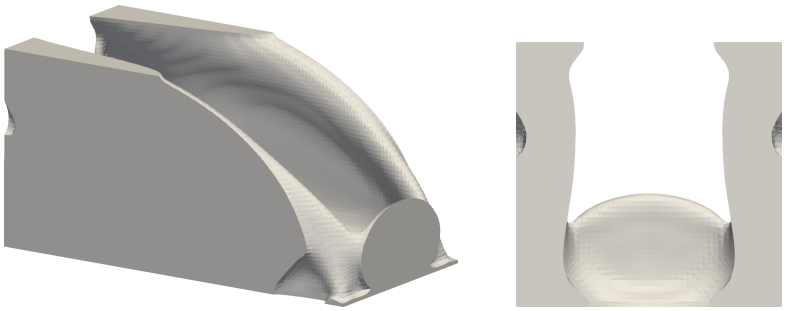

(a) Bird's-eye view (b) Rear view

Figure 12: Optimal structure with the self-support and AM deformation constraints (Proposed method); $J_v/J_{v\ ref} = 118\%$.

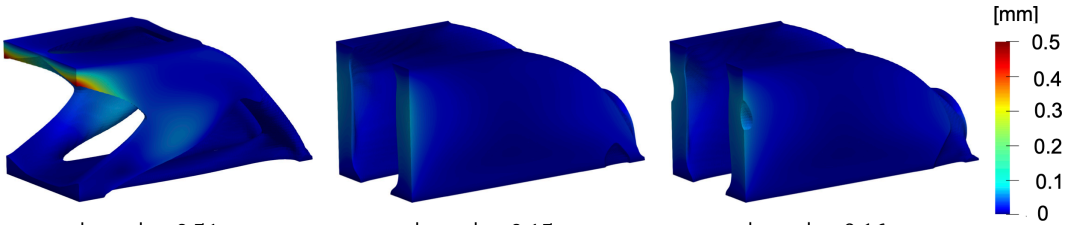

(a) Without constraint

(b) With the self-support and AM deformation constraints (Previous method)

(c) With the self-support and AM deformation constraints (Proposed method)

Figure 13: Comparison of the deformation induced by the building process for the optimized 3D cantilever beam.

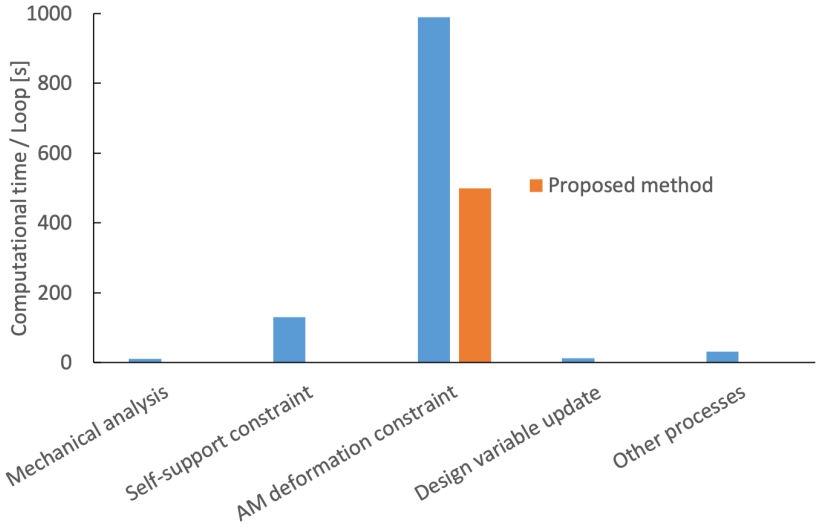

Figure 14: Computational time for each process.

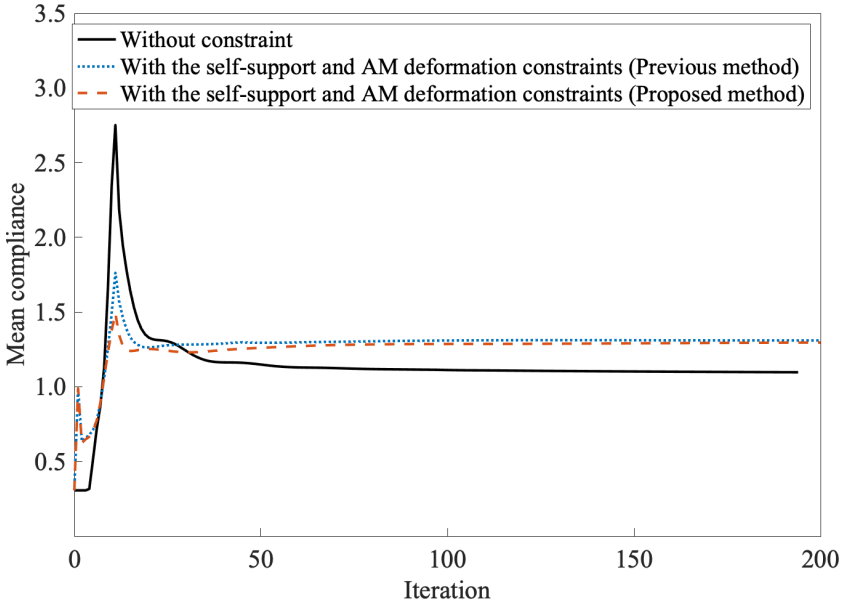

Figure 15: Iteration history of the objective value.

with the same geometric features. Fig. 13 presents the results of the deformations analyzed for optimal structures using the AM process model. Figs. 13(b) and 13(c) illustrate that the proposed method suppresses deformation effectively, comparable to the performance of the previous method. Fig. 14 shows the computational time for each process in the optimization loop. Compared to the two-dimensional numerical result, the computational time for the adjoint analysis is reduced significantly. Because the number of elements is relevant. Therefore, the larger the model with a large number of elements, the more effectively the proposed method can reduce the computational time. Fig. 15 shows the iterative history of the objective function, which indicates that the convergence behavior remains unchanged even with the inclusion of the self-support constraint. Thus, given these results, the proposed method can effectively reduce the computational time of the AM deformation constraints.

8. Conclusion

This paper proposed a computational cost reduction method for the AM deformation constraint in topology optimization. The main contributions of this study are summarized as follows:

1. An AM process model based on the inherent strain method was presented, and the governing equation for the final state of the building process were formulated.
2. A constraint function that suppressed the AM deformation was formulated. Then, we proposed a method to reduce the computational cost of sensitivity analysis using the governing equations that represent the final state of the building process.
3. We formulated an optimization problem with the AM deformation constraint combined with the self-support constraint and constructed an algorithm using FEM.
4. Through numerical examples, we confirmed that the proposed method reduced the computation time for optimization and obtained an optimal structure with the same performance as the previous method.

Acknowledgments

This study was supported by a JSPS grant for Scientific Research (C) JP21K03826.

Statement

During the preparation of this work the author used DeepL and ChatGPT in order to English proofreading. After using this tool, the authors reviewed and edited the content as needed and takes full responsibility for the content of the publication.

References

References

[1] A. T. Gaynor, J. K. Guest, Topology optimization considering overhang constraints: Eliminating sacrificial support material in additive manufacturing through design, Structural and Multidisciplinary Optimization 54 (5) (2016) 1157–1172.

[2] M. Langelaar, Topology optimization of 3d self-supporting structures for additive manufacturing, Additive manufacturing 12 (2016) 60–70.

[3] M. Langelaar, An additive manufacturing filter for topology optimization of print-ready designs, Structural and multidisciplinary optimization 55 (3) (2017) 871–883.

[4] G. Allaire, C. Dapogny, R. Estevez, A. Faure, G. Michailidis, Structural optimization under overhang constraints imposed by additive manufacturing technologies, Journal of Computational Physics 351 (2017) 295–328.

[5] X. Qian, Undercut and overhang angle control in topology optimization: a density gradient based integral approach, International Journal for Numerical Methods in Engineering 111 (3) (2017) 247–272.

[6] Y. Wang, J. Gao, Z. Kang, Level set-based topology optimization with overhang constraint: towards support-free additive manufacturing, Computer Methods in Applied Mechanics and Engineering 339 (2018) 591–614.

[7] E. van de Ven, R. Maas, C. Ayas, M. Langelaar, F. van Keulen, Continuous front propagation-based overhang control for topology optimization with additive manufacturing, Structural and Multidisciplinary Optimization 57 (5) (2018) 2075–2091.

[8] A. Garaigordobil, R. Ansola, J. Santamaría, I. Fernández de Bustos, A new overhang constraint for topology optimization of self-supporting structures in additive manufacturing, Structural and Multidisciplinary Optimization 58 (5) (2018) 2003–2017.

[9] C.-J. Thore, H. A. Grundström, B. Torstenfelt, A. Klarbring, Penalty regulation of overhang in topology optimization for additive manufacturing, Structural and Multidisciplinary Optimization 60 (1) (2019) 59–67.

[10] R. A. Wildman, A. T. Gaynor, Topology optimization for reducing additive manufacturing processing distortions, Tech. rep., Weapons and Materials Research Directorate, US Army Research Laboratory (2017).

[11] G. Allaire, L. Jakabčin, Taking into account thermal residual stresses in topology optimization of structures built by additive manufacturing, Mathematical Models and Methods in Applied Sciences 28 (12) (2018) 2313–2366.

[12] T. Miki, T. Yamada, Topology optimization considering the distortion in additive manufacturing, Finite Elements in Analysis and Design 193 (2021) 103558.

[13] G. Allaire, B. Bogosel, Optimizing supports for additive manufacturing, Structural and Multidisciplinary Optimization 58 (6) (2018) 2493–2515.

[14] M. Zhou, Y. Liu, Z. Lin, Topology optimization of thermal conductive support structures for laser additive manufacturing, Computer Methods in Applied Mechanics and Engineering 353 (2019) 24–43.

[15] C. Wang, X. Qian, Optimizing support for heat dissipation in additive manufacturing, in: International Design Engineering Technical Conferences and Computers and Information in Engineering Conference, Vol. 83983, American Society of Mechanical Engineers, 2020, p. V009T09A018.

[16] T. Miki, S. Nishiwaki, Topology optimization of the support structure for heat dissipation in additive manufacturing, Finite Elements in Analysis and Design 203 (2022) 103708.

[17] R. Ranjan, C. Ayas, M. Langelaar, F. v. Keulen, Controlling local overheating in topology optimization for additive manufacturing, Structural and Multidisciplinary Optimization 65 (6) (2022) 1–21.

[18] L. Papadakis, A. Loizou, J. Risse, J. Schrage, Numerical computation of component shape distortion manufactured by selective laser melting, Procedia Cirp 18 (2014) 90–95.

[19] N. Hodge, R. Ferencz, J. Solberg, Implementation of a thermomechanical model for the simulation of selective laser melting, Computational Mechanics 54 (1) (2014) 33–51.

[20] C. Li, C. Fu, Y. Guo, F. Fang, A multiscale modeling approach for fast prediction of part distortion in selective laser melting, Journal of Materials Processing Technology 229 (2016) 703–712.

[21] T. Mukherjee, W. Zhang, T. DebRoy, An improved prediction of residual stresses and distortion in additive manufacturing, Computational Materials Science 126 (2017) 360–372.

[22] E. R. Denlinger, M. Gouge, J. Irwin, P. Michaleris, Thermomechanical model development and in situ experimental validation of the laser powder-bed fusion process, Additive Manufacturing 16 (2017) 73–80.

[23] M. Chiumenti, E. Neiva, E. Salsi, M. Cervera, S. Badia, J. Moya, Z. Chen, C. Lee, C. Davies, Numerical modelling and experimental validation in selective laser melting, Additive Manufacturing 18 (2017) 171–185.

[24] C. Li, J. Liu, X. Fang, Y. Guo, Efficient predictive model of part distortion and residual stress in selective laser melting, Additive Manufacturing 17 (2017) 157–168.

[25] N. Keller, V. Ploshikhin, New method for fast predictions of residual stress and distortion of am parts, in: Solid Freeform Fabrication Symposium, Vol. 25, 2014.

[26] I. Setien, M. Chiumenti, S. van der Veen, M. San Sebastian, F. Garciandía, A. Echeverría, Empirical methodology to determine inherent strains in additive manufacturing, Computers & Mathematics with Applications 78 (7) (2019) 2282–2295.

[27] Q. Chen, X. Liang, D. Hayduke, J. Liu, L. Cheng, J. Oskin, R. Whitmore, A. C. To, An inherent strain based multiscale modeling framework for simulating part-scale residual deformation for direct metal laser sintering, Additive Manufacturing 28 (2019) 406–418.

[28] X. Liang, Q. Chen, L. Cheng, D. Hayduke, A. C. To, Modified inherent strain method for efficient prediction of residual deformation in direct metal laser sintered components, Computational Mechanics 64 (6) (2019) 1719–1733.

[29] B. C. Prabhune, K. Suresh, A fast matrix-free elasto-plastic solver for predicting residual stresses in additive manufacturing, Computer-Aided Design (2020) 102829.

[30] T. Miki, Self-support topology optimization considering distortion for metal additive manufacturing, Computer Methods in Applied Mechanics and Engineering 404 (2023) 115821.

[31] S. Xu, J. Liu, Y. Ma, Residual stress constrained self-support topology optimization for metal additive manufacturing, Computer Methods in Applied Mechanics and Engineering 389 (2022) 114380.

[32] T. Yamada, K. Izui, S. Nishiwaki, A. Takezawa, A topology optimization method based on the level set method incorporating a fictitious interface energy, Computer Methods in Applied Mechanics and Engineering 199 (45-48) (2010) 2876–2891.

[33] M. Bihr, G. Allaire, X. Betbeder-Lauque, B. Bogosel, F. Bordeu, J. Querois, Part and supports optimization in metal powder bed additive manufacturing using simplified process simulation, Computer Methods in Applied Mechanics and Engineering 395 (2022) 114975.

[34] M. Bugatti, Q. Semeraro, Limitations of the inherent strain method in simulating powder bed fusion processes, Additive Manufacturing 23 (2018) 329–346.

[35] F. Hecht, New development in freefem++, J. Numer. Math. 20 (3-4) (2012) 251–265.
URL `https://freefem.org/`

[36] G. Allaire, F. Jouve, A.-M. Toader, Structural optimization using sensitivity analysis and a level-set method, Journal of Computational Physics 194 (1) (2004) 363–393.